

Scalable Neural Decoder for Topological Surface Codes

Kai Meinerz, Chae-Yeon Park, and Simon Trebst

Institute for Theoretical Physics, University of Cologne, 50937 Cologne, Germany

(Dated: February 28, 2025)

With the advent of noisy intermediate-scale quantum (NISQ) devices, practical quantum computing has seemingly come into reach. However, to go beyond proof-of-principle calculations, the current processing architectures will need to scale up to larger quantum circuits which in turn will require fast and scalable algorithms for quantum error correction. Here we present a neural network based decoder that, for a family of stabilizer codes subject to depolarizing noise, is scalable to tens of thousands of qubits (in contrast to other recent machine learning inspired decoders) and exhibits faster decoding times than the state-of-the-art union find decoder for a wide range of error rates (down to 1%). The key innovation is to autodecode error syndromes on small scales by shifting a preprocessing window over the underlying code, akin to a convolutional neural network in pattern recognition approaches. We show that such a preprocessing step allows to effectively reduce the error rate by up to two orders of magnitude in practical applications and, by detecting correlation effects, shifts the actual error threshold to $p_{\text{threshold}} = 0.167(0)$, some ten percent higher than the threshold of conventional error correction algorithms such as union find or minimum weight perfect matching. An in-situ implementation of such machine learning-assisted quantum error correction will be a decisive step to push the entanglement frontier beyond the NISQ horizon.

Introduction.— In quantum computing, recent years have seen a paradigm shift which has pivoted experimental roadmaps from building devices of a few pristine qubits towards the realization of circuit architectures of 50-100 qubits but tolerating a significant level of imperfections – the advent of what has been termed noisy intermediate-scale quantum (NISQ) technology [1]. This move has enabled a fundamental success in the recent demonstration that such a NISQ quantum processor is capable of exhibiting a true “quantum advantage” over classical computing resources [2]. One of the leading NISQ platforms involves arrays of superconducting charge qubits, so-called transmons [3], which by design are particular resilient with regard to charge fluctuations. However, building larger quantum circuits from transmons comes with some intricate challenges [4, 5] and will eventually mandate to incorporate quantum error correction (QEC) schemes [6]. Arguably the most promising approach here is the implementation of a surface code [7, 8], which exploits topological properties of the system and, at the same, remains experimentally feasible [9, 10]. In practical settings, one downside of realizing such surface code architectures is the relatively slow decoding time of current quantum error correction codes.

The decoding step in quantum error correcting codes requires, at its core, a *classical* algorithm that efficiently infers the locations of errors from measured error syndromes [11]. The most widely adopted algorithm for this purpose is minimum weight perfect matching (MWPM) [12], an algorithm which runs in polynomial time and is known to nearly achieve the optimal threshold for the independent noise model [13, 14] (a characteristic which does not hold for more general noise models, though). One of the drawbacks of the MWPM algorithm, however, is that its implementations are often simply too slow [15] even for the current generation of superconducting qubits. To improve the algorithmic scaling and to push error thresholds for more general noise situations, a number of alternative decoding approaches have been suggested, of which the most notable might be the renormalization group (RG) [16–18] and union-find (UF) [19] decoders. The RG de-

coder runs, for a surface code in a two-dimensional geometry of linear size L , in $O(L^2 \log L)$ time, often a significant improvement over the MWPM approach (which, in the worst case, scales cubic in the number of errors and thus $O(L^6)$ in system size). However, its threshold value of ~ 0.129 for depolarizing noise [16] is lower than that of the MWPM algorithm (~ 0.151 [14]). The most efficient conventional algorithm is the recently developed UF decoder which runs in $O(L^2)$, i.e. almost linear in the number of qubits, with a threshold ~ 0.146 for the depolarizing noise model (see below) [20]. In addition, the last two years have seen a flurry of activity to adopt machine learning (ML) techniques to best the decoding times and threshold values of these ‘conventional’ algorithms [21–31]. As ML methods can be easily parallelized and generally offer a high degree of adaptability, one might easily accept their potential, but the first practical ML-based decoders have typically delivered only on one of the two benchmarks – improving the error threshold at the expense of scalability or the other way round, providing good scalability but leading to error thresholds which are sometimes even *below* those of the conventional algorithms outlined above [32].

It is the purpose of this paper to introduce a powerful two-step decoding algorithm that combines neural network based preprocessing and union-find decoding to simultaneously achieve (i) improved error thresholds for depolarizing noise, (ii) algorithmic scalability up to tens of thousands of qubits, and (iii) real-life wall-clock run times that, for a wide range of error rates, best even those of the bare union-find algorithm, as summarized in Table I. Our main algorithmic idea can be described as a ‘divide-and-conquer’ approach that employs an ML decoder to preprocess *local* error corrections and leave the unresolved longer-range errors to a conventional UF decoding. The preprocessing step shifts a two-dimensional subsystem mask over a given stabilizer code (akin to the preprocessing in a convolutional neural network often employed in image processing) and decodes local errors in these subsystems. After this step, the system still exhibits errors that require longer range corrections, for which we employ a con-

algorithm	p_{th}	$t_{p=0.01}$	$t_{p=0.05}$	$t_{p=0.1}$	$t_{p=0.1461}$
7×7 ML + UF	0.167(0)	10.5	25.1	43.4	78.6
5×5 ML + UF	0.162(5)	6.7	12.8	26.2	56.2
UF	0.146(1)	8.4	22.5	44.9	92.8
7×7 ML + MWPM	0.167(1)	~ 210	~ 530	~ 650	~ 980
MWPM	0.154(2)	~ 560	~ 840	~ 1100	~ 1300

Table I. Overview of results. For a number of variants of our decoding algorithm we provide the error threshold p_{th} for depolarizing noise (2nd column) as well as wall-clock time measurements (in milliseconds) of the decoding time for different error rates (averaged over 10^6 instances) for the lattice size is $L = 255$. The bold-faced entries identify the best performing algorithm when optimizing for error threshold or compute times. Comparison is shown for the union-find (UF) and minimum weight perfect matching (MWPM) decoders, improved with machine learning (ML) bases preprocessing using 5×5 or 7×7 subsystem masks (see main text). We have used a custom implementation for the UF decoder [33] and PyMatching [34] for the MWPM. The details of our CPU/GPU setup are provided in Appendix B.

ventional UF decoder. However, since the preprocessing reduces the effective error rate – up to two orders of magnitude depending on the original error rate – this second step is extremely performant when compared with employing UF decoding to the original error instances. Extensive wall-clock time measurements of our approach (the true performance indicator in many real-life applications) show that our algorithm outperforms the bare UF decoder both in the low-noise regime (down to error rates as low as 1%) in which one ideally wants to operate quantum computing devices as well as the high-noise regime where our ML-assisted approach is found to push the error threshold by up to 10% above the value of the bare UF decoder.

Divide and Conquer QEC.— Throughout the paper, we apply our decoding algorithm to the toric code in the presence of depolarizing noise, albeit our approach is more generally applicable also to other topological codes and noise models. We consider a standard setup, where the toric code is defined on a square lattice of size $L \times L$ and the stabilizer operators around the vertices and plaquettes are given by $X_v = \prod_{i \in v} X_i$ and $Z_p = \prod_{i \in p} Z_i$. The code space is then spanned by the basis vectors $\{|\psi\rangle : X_v |\psi\rangle = 1 \forall v, Z_p |\psi\rangle = 1 \forall p\}$, which, for periodic boundary conditions, is 4 dimensional (and thus encodes 2 qubits) and the distance of the code (i.e. the minimum length of a Pauli string that transforms one state in the code space to another state) is L . Each Z (X) error on a qubit (located on the edges of the lattice) flips the value of the nearby X_v (Z_p) operators.

The decoding problem is then defined as identifying the error configuration for a given syndrome, i.e. a given measurement of the outcomes of all stabilizers X_v and Z_p . To do so, we employ a two-stage ‘divide-and-conquer’ procedure. In the first stage – the ML-assisted preprocessing – we aim to remove those errors that can be inferred from *local* syndromes. To this end, we only consider qubits directly connected to so-called defects (identified by an odd syndrome measurement $X_v = -1$ or $Z_p = -1$), as they are the typical source of locally correctable errors. To infer which error is the most prob-

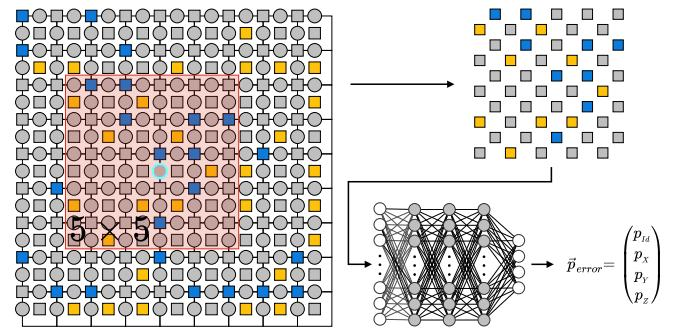


Figure 1. Construction of the input data and neural network. A single qubit (cyan circle) is selected as the reference point of the construction. All syndromes in the immediate vicinity (red square) are used as the input, whereby measured syndromes (blue/yellow) are assigned the value $+1/-1$ and not measured syndromes (grey) are assigned value 0, respectively. Passing the input through the feed forward network results in the error probabilities of the initially selected qubit.

able for a given qubit, our preprocessing step shifts through all qubits with a subsystem mask of size $L_{\text{input}} \times L_{\text{input}}$ centered around an ‘examination qubit’ located at its center (see the setup in Fig. 1). The local inference task for each such examination qubit is then assigned to a neural network, whose details we discuss below. The result of this step is that a large number of local errors are decoded and only a small fraction of non-local errors, manifest on scales beyond the range of our subsystem mask, remain.

The second stage of our algorithm thus is to process these remaining non-local errors, which are left after updating the syndromes using the local error decoding in the previous stage. To do so, we employ a conventional UF decoder on the remaining syndrome. Doing so is significantly more efficient than employing the UF decoder on the bare decoding problem (without the preprocessing), as we will see that the effective error rate for this UF decoding step is up to two orders of magnitude smaller than the original error rate (see the results section below).

Neural decoder.— At the heart of our divide-and-conquer QEC approach is a neural network that decodes error syndromes within a local subsystem mask, as illustrated in Fig. 1. We train this neural network to output the most probable error (among the four possible $\{I, X, Y, Z\}$ errors) of the central qubit given $2L_{\text{input}}^2$ nearby syndromes as an input (with the factor of 2 coming from the two types of X and Z measurements). In machine learning, this type of task is commonly known as multiclass classification problem and exceedingly well-studied in the context of supervised learning approaches (e.g. in image classification). To adopt such a supervised learning approach to optimize our neural network, we do training with a labeled dataset, i.e. batches of error-syndrome pairs generated for a given error rate (and noise model). In doing so, we use the error of each qubit directly touching a defect (as in the inference step outlined above) as a label and X , Z syndromes of size $L_{\text{input}} \times L_{\text{input}}$ surrounding this qubit as input. In practice, we train our networks in 10^6 epochs,

for which we create independent sets of 512 error-syndrome batches “on the fly”, which also reduces the chance of overfitting.

In designing the neural network architecture, we realize that there is an inherent trade-off between the two hierarchical algorithmic layers of our divide-and-conquer approach: If one opts for a small neural network, its computation time remains low but its accuracy in resolving local syndromes drops, resulting in more computational load for the UF decoder on the higher algorithmic layer. If, on the other hand, one opts for a large neural network, its accuracy in resolving syndromes goes up at the cost of larger compute times, while also alleviating the load of the higher-level UF decoder. Indeed, this trade off leads to a sweet spot, i.e. an intermediate neural network size that results, e.g., in minimal wall-clock run times *or* maximal error thresholds. To identify an optimal configuration, we have explored a multitude of different network architectures, varying the size of the subsystem mask, the depth of the network, and the number of nodes per layer as main parameters (as detailed in Appendix A). When optimizing for compute speed a 5×5 subsystem mask turns out to be ideal, while pushing the error threshold one might want to go with a 7×7 subsystem mask – see Table I. However, since the error threshold of the speed-optimized network is only 3% smaller than the threshold-optimized network, we consider the 5×5 neural network approach the best compromise in achieving fast decoding *and* high error thresholds for an algorithm that *also* delivers on high scalability.

Benchmark results.— In benchmarking our divide-and-conquer QEC algorithm, we start in the high-noise regime and calculate the error threshold of our approach. Decoding 10^6 random instances of depolarized noise for different error rates and linear system sizes in the range $L = 7, \dots, 127$ we can readily deduce the error threshold from the finite-size scaling shown in Fig. 2. In comparison to the bare UF algorithm (top panel), which exhibits an error threshold of $p_{\text{th}}^{\text{UF}} = 0.1461 \pm 0.0005$, our algorithm yields a 10% higher value of $p_{\text{th}} = 0.1625 \pm 0.0003$ (when we employ a 5×5 subsystem mask). This notable increase of the error threshold indicates that our ML-assisted approach is capable of identifying and resolving *correlated* errors in the depolarized noise, which the bare UF decoder cannot handle. We found that one can slightly push this threshold value even further up (at the expense of additional compute time) by employing a larger 7×7 subsystem mask, which gives $p_{\text{th}} = 0.1670 \pm 0.0006$ (see also Table I). Going to even larger subsystem masks has not resulted in any further notable improvement of the threshold value in our measurements. It should be noted that our threshold value is higher than the one of the bare RG decoder [16] with $p_{\text{th}}^{\text{RG}} = 0.153$ and comparable to those found for a combination of RG and sparse decoders [18], or the best ML-based decoders using deep neural networks, for which error thresholds of $p_{\text{th}}^{\text{ML}} \approx 0.165$ are reported [23, 28] for depolarized noise. However, our result is still significantly below the optimal value of $p_{\text{th}} = 0.189(3)$, inferred from a mapping of the decoding problem to the classical disordered eight-vertex Ising model [35]. In accordance with this mapping, we observe a critical exponent $\nu = 1.5(4)$ for the data collapse (see

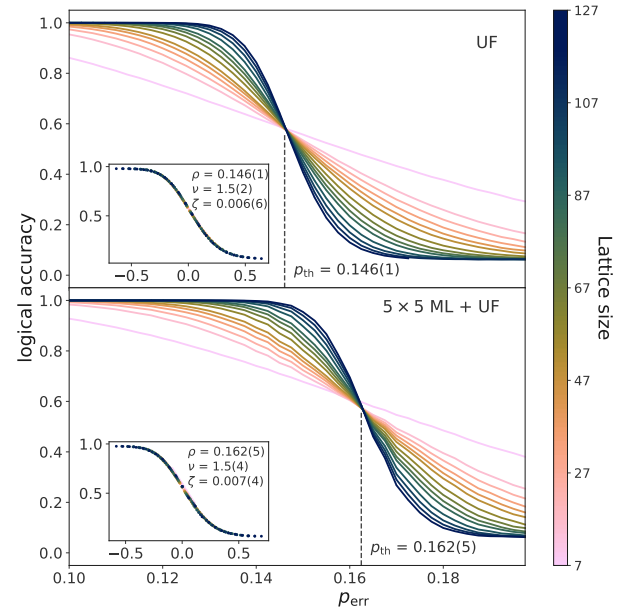


Figure 2. **Error threshold and scaling behavior** for the conventional union find (UF) algorithm (upper panel), and the machine learning assisted union find (ML+UF) algorithm (lower panel) for depolarized noise. The ML assisted algorithm shifts the error threshold by some 10%, from $p_{\text{err}} = 0.146(1)$ for the UF to $p_{\text{err}} = 0.162(5)$ for the ML+UF algorithm. The insets show a data collapse around these threshold values for different system sizes, consistently yielding a critical exponent of $\nu = 1.5(3)$.

insets of Fig. 2) in good agreement with numerical studies of the critical behavior at the Nishimori point of the random bond Ising model [36–38] relevant for the decoding problem.

One particularly notable measure to illustrate the inner workings of our divide-and-conquer approach is the ‘effective error rate’, i.e. the reduction of errors obtained after performing the first step of our algorithm – the preprocessing using a subsystem mask and neural network-based local decoding. Shown in Fig. 3, this effective error rate reveals that this preprocessing step is particularly powerful at low error rates, i.e.

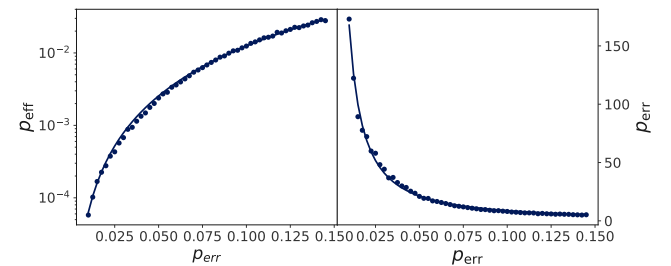


Figure 3. **Effective error reduction** attained by the ML preprocessing step of our divide-and-conquer algorithm. The left panel shows the effective error rate p_{eff} as a function of the original error probability p_{err} , illustrating the effect of local decodings in the preprocessing step. The right panel shows the ratio of the original error probability and the effective error rate.

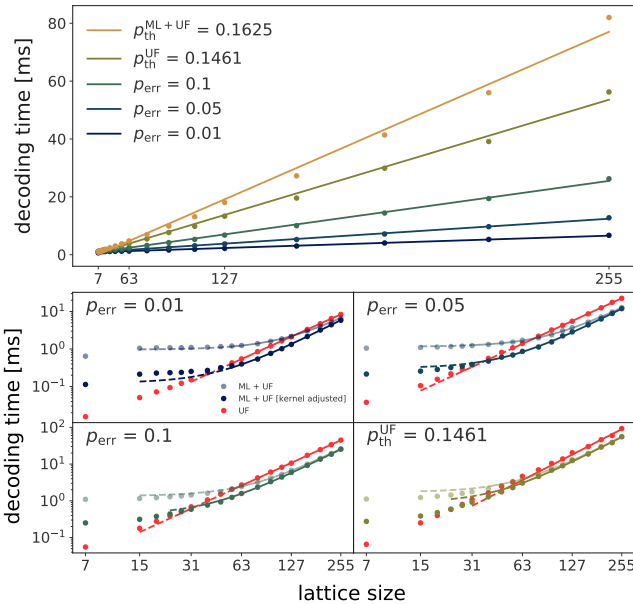


Figure 4. **Algorithmic scaling** of our divide-and-conquer decoder for various error rates (top panel). The bottom panels show detailed comparisons with the bare UF decoder on a log-log scale. Shown in all panels is the average decoding time measured in wall clock time averaged over 10^6 error instances. The ‘kernel adjusted’ time in the lower panels is the ML+UF decoding time subtracted by a constant offset, to compensate kernel launch times (see main text). The crossing points at which the ML+UF decoder outperforms the bare UF decoder is shown in Fig. 5.

in the regime where few long-range errors occur. Here one can reduce the initial error rate by more than two orders of magnitude (see the right panel of Fig. 3), thereby significantly speeding up the subsequent UF decoding step (as compared to a direct application to the original syndrome).

As such one might naively expect the biggest computing gain of our algorithm in the low-noise regime. For practical implementations this is, however, not true as becomes apparent when performing run time measurements of our decoder. Such measurements are illustrated in Fig. 4 where the decoding time (again averaged over 10^6 error instances) is plotted versus the linear system size for different error rates. The top panel nicely demonstrates that, for large system sizes, we find near linear scaling for both the UF and our divide-and-conquer UF+ML decoder, independent of the error rate. Note that our ML-assisted decoder easily scales up to $2 \times 255 \times 255 \approx 130,000$ qubits where the decoding time per instance is still a fraction of a second – this should be contrasted to other ML-based decoders reported in the literature, which could not be scaled beyond a hundred qubits (see the overview in Table V of the Appendix).

If we look at the scaling of our algorithm for small to moderate system sizes (highlighted in the lower panels of Fig. 4), a breakdown of the linear scaling of the ML-assisted decoder becomes evident. There is indeed a considerable ‘lag’ in our implementation of our divide-and-conquer approach, which arises from the usage of an external GPU to perform the neu-

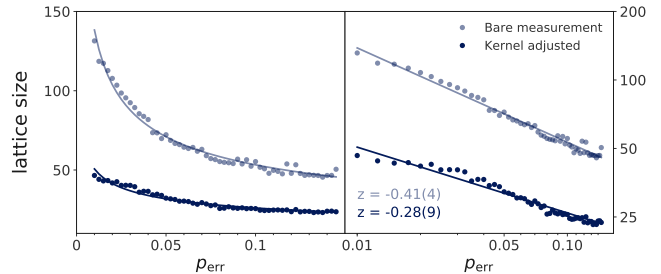


Figure 5. **Crossing point of decoding time** of ML+UF decoder and the UF decoder. Shown is the lattice size, at which the decoding time of the bare UF decoder becomes greater than those of the ML+UF decoder in Fig. 4. The right panel shows the same data on a double logarithmic scale, indicating a power-law decrease with exponents as indicated in the figure.

ral network-based preprocessing step (see Appendix B for detailed specifications of our setup). Doing so readily implies another inherent trade off: Initializing the neural network and loading the syndrome data to the GPU component has an almost constant overhead, which explains the plateau in our scaling plots for small system sizes where the advantage of fast GPU processing of the neural network is not compensating this overhead (as it is the case for large system sizes). Performing careful measurements of this ‘kernel start-up’ time, we can subtract parts of this overhead, which would not exist in a dedicated or in-situ device in a practical implementation of QEC in the lab, to arrive at the alternate scaling curve labeled ‘kernel adjusted’ in Fig. 4.

For both types of compute time measurements, we find a crossing point, indicating an intermediate-scale system size at which the ML-assisted decoder outperforms the bare UF decoder. This critical system size is plotted as a function of the error rate in Fig. 5 above. For small error rates this critical system size is found to follow a power-law decrease reaching a relatively modest system size $L \sim 25$ for error rates around 10%. Bearing in mind that an *in-situ* implementation of our decoder to perform QEC in an actual device should benefit from dedicated hardware (with no overheads), this should further advance the performance of our approach and put it onto the roadmap of future quantum device architecture with 100-1000 of qubits.

In summary, we have demonstrated that the combination of machine-learning assisted preprocessing in conjunction with conventional decoders in a newly devised divide-and-conquer approach results in a vastly scalable algorithm. Our practical implementation shows a significant reduction of actual decoding times (to a few milliseconds in our hardware setup), while also pushing the error threshold by resolving correlated errors.

Acknowledgments.— We thank M. Kastoryano and T. Wagner for insightful discussions. This project was funded by the Deutsche Forschungsgemeinschaft under Germany’s Excellence Strategy - Cluster of Excellence Matter and Light for Quantum Computing (ML4Q) EXC 2004/1 - 390534769 and within the CRC network TR 183 (project grant 277101999) as part of project B01.

Note added.— In the days prior to submission of this manuscript a tensor network decoder has been introduced [39], for which an error threshold for depolarizing noise in

the toric code of $p_{\text{th}} = 0.1881(3)$ is reported, indistinguishable within error bars from the upper bound inferred from a mapping of the decoding problem to the classical disordered eight-vertex Ising model [35].

[1] J. Preskill, Quantum Computing in the NISQ era and beyond, *Quantum* **2**, 79 (2018).

[2] F. Arute, K. Arya, R. Babbush, D. Bacon, J. C. Bardin, R. Barends, R. Biswas, S. Boixo, F. G. S. L. Brandao, D. A. Buell, B. Burkett, Y. Chen, Z. Chen, B. Chiaro, R. Collins, W. Courtney, A. Dunsworth, E. Farhi, B. Foxen, A. Fowler, C. Gidney, M. Giustina, R. Graff, K. Guerin, S. Habegger, M. P. Harrigan, M. J. Hartmann, A. Ho, M. Hoffmann, T. Huang, T. S. Humble, S. V. Isakov, E. Jeffrey, Z. Jiang, D. Kafri, K. Kechedzhi, J. Kelly, P. V. Klimov, S. Knysh, A. Korotkov, F. Kostritsa, D. Landhuis, M. Lindmark, E. Lucero, D. Lyakh, S. Mandrà, J. R. McClean, M. McEwen, A. Megrant, X. Mi, K. Michielsen, M. Mohseni, J. Mutus, O. Naaman, M. Neeley, C. Neill, M. Y. Niu, E. Ostby, A. Petukhov, J. C. Platt, C. Quintana, E. G. Rieffel, P. Roushan, N. C. Rubin, D. Sank, K. J. Satzinger, V. Smelyanskiy, K. J. Sung, M. D. Trevithick, A. Vainsencher, B. Villalonga, T. White, Z. J. Yao, P. Yeh, A. Zalcman, H. Neven, and J. M. Martinis, Quantum supremacy using a programmable superconducting processor, *Nature* **574**, 505 (2019).

[3] J. Koch, T. M. Yu, J. Gambetta, A. A. Houck, D. I. Schuster, J. Majer, A. Blais, M. H. Devoret, S. M. Girvin, and R. J. Schoelkopf, Charge-insensitive qubit design derived from the Cooper pair box, *Phys. Rev. A* **76**, 042319 (2007).

[4] D. Willsch, M. Nocon, F. Jin, H. De Raedt, and K. Michielsen, Gate-error analysis in simulations of quantum computers with transmon qubits, *Phys. Rev. A* **96**, 062302 (2017).

[5] C. Berke, E. Varvelis, S. Trebst, A. Altland, and D. P. DiVincenzo, Transmon platform for quantum computing challenged by chaotic fluctuations, (2020), arXiv:2012.05923.

[6] D. Gottesman, An introduction to quantum error correction and fault-tolerant quantum computation, *Proceedings of Symposia in Applied Mathematics* **68**, 13 (2010).

[7] A. Y. Kitaev, Fault-tolerant quantum computation by anyons, *Annals of Physics* **303**, 2 (2003).

[8] S. B. Bravyi and A. Y. Kitaev, Quantum codes on a lattice with boundary, arXiv preprint quant-ph/9811052 (1998).

[9] A. G. Fowler, M. Mariantoni, J. M. Martinis, and A. N. Cleland, Surface codes: Towards practical large-scale quantum computation, *Phys. Rev. A* **86**, 032324 (2012).

[10] C. K. Andersen, A. Remm, S. Lazar, S. Krinner, N. Lacroix, G. J. Norris, M. Gabureac, C. Eichler, and A. Wallraff, Repeated quantum error detection in a surface code, *Nature Physics* **16**, 875 (2020).

[11] D. Gottesman, *Stabilizer codes and quantum error correction*, Ph.D. thesis, California Institute of Technology (1997).

[12] J. Edmonds, Path, Trees, and Flowers, *Canadian Journal of Mathematics* **17**, 449 (1965).

[13] E. Dennis, A. Kitaev, A. Landahl, and J. Preskill, Topological quantum memory, *Journal of Mathematical Physics* **43**, 4452 (2002).

[14] J. W. Harrington, *Analysis of quantum error-correcting codes: symplectic lattice codes and toric codes*, Ph.D. thesis, California Institute of Technology (2004).

[15] An impressive optimization of an MWPM implementation has recently been reported using a local variant of the matching decoder [40] in form of the PyMatching package [34], which we use for benchmarking purposes throughout this manuscript.

[16] G. Duclos-Cianci and D. Poulin, Fast decoders for topological quantum codes, *Phys. Rev. Lett.* **104**, 050504 (2010).

[17] G. Duclos-Cianci and D. Poulin, in *2010 IEEE Information Theory Workshop* (2010) pp. 1–5.

[18] G. Duclos-Cianci and D. Poulin, Fault-Tolerant Renormalization Group Decoder for Abelian Topological Codes, *Quantum Info. Comput.* **14**, 721 (2014).

[19] N. Delfosse and N. H. Nickerson, Almost-linear time decoding algorithm for topological codes, (2017), arXiv:1709.06218.

[20] It has been claimed that parallelized versions of the MWPM [41] or RG decoders [16] can achieve faster than linear decoding time. However, algorithmic scaling of such parallelized algorithms has been discussed in mostly theoretical terms and not demonstrated under realistic conditions yet (e.g. by measuring wall-clock times as done in this manuscript). In particular, we believe that resolving data dependencies will remain a significant bottleneck in any *practical implementation* of the proposed parallelized algorithms.

[21] S. Varsamopoulos, B. Criger, and K. Bertels, Decoding small surface codes with feedforward neural networks, *Quantum Science and Technology* **3**, 015004 (2017).

[22] G. Torlai and R. G. Melko, Neural Decoder for Topological Codes, *Phys. Rev. Lett.* **119**, 030501 (2017).

[23] S. Krastanov and L. Jiang, Deep neural network probabilistic decoder for stabilizer codes, *Scientific Reports* **7**, 11003 (2017).

[24] P. Baireuther, M. D. Caio, B. Criger, C. W. J. Beenakker, and T. E. O’Brien, Neural network decoder for topological color codes with circuit level noise, *New Journal of Physics* **21**, 013003 (2019).

[25] Y.-H. Liu and D. Poulin, Neural belief-propagation decoders for quantum error-correcting codes, *Phys. Rev. Lett.* **122**, 200501 (2019).

[26] P. Andreasson, J. Johansson, S. Liljestrand, and M. Granath, Quantum error correction for the toric code using deep reinforcement learning, *Quantum* **3**, 183 (2019).

[27] T. Wagner, H. Kampermann, and D. Bruß, Symmetries for a high-level neural decoder on the toric code, *Phys. Rev. A* **102**, 042411 (2020).

[28] D. Fitzek, M. Eliasson, A. F. Kockum, and M. Granath, Deep Q-learning decoder for depolarizing noise on the toric code, *Phys. Rev. Research* **2**, 023230 (2020).

[29] L. Domingo Colomer, M. Skotiniotis, and R. Muñoz-Tapia, Reinforcement learning for optimal error correction of toric codes, *Physics Letters A* **384**, 126353 (2020).

[30] X. Ni, Neural Network Decoders for Large-Distance 2D Toric Codes, *Quantum* **4**, 310 (2020).

[31] R. Sweke, M. S. Kesselring, E. P. L. van Nieuwenburg, and J. Eisert, Reinforcement learning decoders for fault-tolerant quantum computation, *Machine Learning: Science and Technology* **2**, 025005 (2020).

- [32] We provide a snapshot of the current status of ML-based decoders in Appendix E, which provides detailed performance benchmarks and allows for direct comparisons of various approaches.
- [33] C.-Y. Park and K. Meinerz, Open-source C++ implementation of the Union-Find decoder, <https://github.com/chaeyeun-park/UnionFind> .
- [34] O. Higgott and N. P. Breuckmann, PyMatching, <https://pymatching.readthedocs.io/> .
- [35] H. Bombin, R. S. Andrist, M. Ohzeki, H. G. Katzgraber, and M. A. Martin-Delgado, Strong Resilience of Topological Codes to Depolarization, *Phys. Rev. X* **2**, 021004 (2012).
- [36] A. Honecker, M. Picco, and P. Pujol, Universality Class of the Nishimori Point in the 2D $\pm J$ Random-Bond Ising Model, *Phys. Rev. Lett.* **87**, 047201 (2001).
- [37] F. Merz and J. T. Chalker, Negative scaling dimensions and conformal invariance at the Nishimori point in the $\pm J$ random-bond Ising model, *Phys. Rev. B* **66**, 054413 (2002).
- [38] H. G. Katzgraber, H. Bombin, and M. A. Martin-Delgado, Error Threshold for Color Codes and Random Three-Body Ising Models, *Phys. Rev. Lett.* **103**, 090501 (2009).
- [39] C. T. Chubb, General tensor network decoding of 2D Pauli codes, (2021), arXiv:2101.04125.
- [40] O. Higgott and N. P. Breuckmann, Subsystem codes with high thresholds by gauge fixing and reduced qubit overhead, (2020), arXiv:2010.09626.
- [41] A. G. Fowler, Minimum weight perfect matching of fault-tolerant topological quantum error correction in average $\mathcal{O}(1)$ parallel time, *Quantum Info. Comput.* **15**, 0145 (2015).
- [42] TensorFlow, <https://github.com/tensorflow/tensorflow> .
- [43] H. N. Gabow, *Implementation of Algorithms for Maximum Matching on Nonbipartite Graphs.*, Ph.D. thesis, Stanford University (1974).
- [44] E. L. Lawler, *Combinatorial Optimization: Networks and Matroids* (Holt, Rinehart, and Winston, 1976).
- [45] A. G. Fowler, A. C. Whiteside, and L. C. Hollenberg, Towards practical classical processing for the surface code, *Phys. Rev. Lett.* **108**, 180501 (2012).
- [46] N. Delfosse and G. Zémor, Linear-time maximum likelihood decoding of surface codes over the quantum erasure channel, *Phys. Rev. Research* **2**, 033042 (2020).

Appendix A: Neural Networks

This appendix provides a detailed overview of the tested network architectures to find an optimal decoding setup, along with an expose of the hyperparameters used in the training of the neural network(s).

Network Architecture

In order to optimize our divide-and-conquer algorithm to simultaneously achieve minimal wall-clock run times and high error thresholds, while remaining scalable, we have explored a multitude of different network architectures, varying the size of the subsystem mask, the depth of the network, and the number of nodes per layer as main parameters. A systematic overview of some of the tested network architectures is provided in Table II below.

hidden layers	hidden nodes	total parameters		
		$L_{\text{input}} = 3$	$L_{\text{input}} = 5$	$L_{\text{input}} = 7$
1	32	740	1764	3300
1	64	1476	3526	6596
1	128	2948	7044	13188
1	256	5892	14084	26372
2	32	1796	2820	4356
2	64	5636	7684	10756
2	128	19460	23556	29700
2	256	71684	79876	92164
3	32	2852	3876	5412
3	64	9796	11844	14916
3	128	35972	40068	46212
3	256	137476	145668	157956

Table II. **Overview of neural network architectures** tested to solely optimize the wall-clock run time by varying the size of the $L_{\text{input}} \times L_{\text{input}}$ subsystem mask (see Fig. 1 of the main text), the number of hidden layers, and nodes per layer. The optimal configuration is highlighted in bold-face. Note that when trying to solely maximizing the error threshold, a different network architecture is singled out as ideal (see main text).

5 \times 5 network parameters (optimal wall-clock time)	
hidden layers	3
hidden nodes per layer	128
total number free parameter	40 068
activation functions hidden layer	Relu
activation functions output layer	Softmax

7 \times 7 network parameters (optimal error threshold)	
hidden layers	5
hidden nodes per layer	512
total number free parameter	1 103 364
activation functions hidden layer	Relu
activation functions output layer	Softmax

Table III. **Optimized network architectures.** The upper panel provides detailed parameters for a speed-optimized decoder (minimizing the wall-clock time), based on a 5×5 subsystem neural network. The lower panel provides parameters for a threshold-optimized decoder, based on a 7×7 subsystem neural network.

As discussed in the main text, our divide-and-conquer approach has an inherent trade off between the two hierarchical algorithmic layers: If one opts for a small neural network, its computation time remains low but its accuracy in resolving syndromes drops, resulting in more computational load for the UF decoder on the higher level. If, on the other hand, one opts for a large neural network, its accuracy in resolving syndromes goes up at the cost of larger compute times, while also alleviating the load of the higher-level UF decoder. Indeed, this trade off leads to a sweet spot, i.e. an intermediate neural network size that results, e.g., in optimal compute time.

If our goal is to optimize for *decoding speed*, i.e. minimizing the wall-clock time measured for decoding 10^6 random instances for a toric code with linear system size $L = 255$ (corresponding to the values listed in Table I of the main manuscript), we find that among the multitude of different network architectures listed in Table II, the 5×5 neural network

training parameters	
batch size	512
epochs	10^6
learning rate	0.001
optimizer	ADAM
loss function	categorical cross-entropy
training lattice size L_{train}	7
section distance L_{input}	5

Table IV. **Hyperparameters** used for the training of our various network architectures. An epoch corresponds to the number of generated training batches (see text).

with 3 hidden layers and 128 nodes per layer (resulting in a total of 40068 adjustable parameters) is the best choice (see also Table IV).

If, on the other hand, our goal is to optimize the *decoding efficiency*, i.e. maximizing the error threshold, then we find that a 7×7 neural network with 5 hidden layers and 512 nodes per layer (resulting in more than 10^6 adjustable parameters in total) is the most favorable network configuration.

However, we note that the error threshold of the speed-optimized network already comes in at $p_{\text{th}} = 0.162(5)$ and as such is only slightly smaller than the maximal threshold of $p_{\text{th}} = 0.167(0)$, which we find for the efficiency-optimized network – in particular when comparing this to the threshold values of the conventional decoders (with error thresholds around $p_{\text{th}} \approx 0.150 \pm 0.004$) and the ideal threshold $p_{\text{th}} = 0.189$ inferred from a mapping of the decoding problem to the classical disordered eight-vertex Ising model [35]. As such, we conclude that the speed-optimized 5×5 neural network already presents a good compromise in achieving fast decoding and high error thresholds for an algorithm that also delivers on high scalability.

Training

Each neural network configuration has been trained using standard supervised learning techniques, using labeled data sets of syndromes and their corresponding underlying errors for a given error rate. Because such error-syndromes pairs can be generated in very efficient ways, we have generated, for every epoch of the training, a new set of 512 such pairs “on the fly”. In effect, this procedure increases the size of the training dataset to be of the order “batch size \times training epochs”, and significantly reduces the chance of overfitting. Detailed training parameters are provided in Table IV, which have been optimized (via a grid search) for the error threshold probability of the decoder and then employed to every training process regardless of the underlying error probability.

Appendix B: Benchmarking

In performing our wall-clock run time benchmarks to provide a measure for real-life applicability we have employed a hardware setup based on the following CPU/GPU tandem

- CPU: Intel Xeon CPU E5-2699A v4 @ 2.40GHz,
- GPU: Nvidia Tesla V100 SXM2.

The times measured are the bare times needed to decode a given syndrome and apply the error correction. As discussed in the main text, our GPU-assisted calculations for the machine learning parts include a ‘kernel time’, i.e. the time needed to launch the CUDA and TensorFlow [42] kernel, every time a syndrome is decoded. We estimate this kernel time as the GPU time needed to run a neural network with subsystem mask $L_{\text{input}} = 7$ for a relatively small error rate of $p_{\text{err}} = 0.01$, where the kernel launch times dominates over the data transfer time and actual GPU calculation time.

Appendix C: Minimum Weight Perfect Matching (MWPM)

To make this manuscript self-contained, we also provide an error threshold calculation of the minimum weight perfect matching (MWPM) decoder for the depolarized noise model using PyMatching [34] – a particularly efficient implementation of MWPM decoder. The most widely used MWPM algorithm for general graphs is the one by Edmonds [12], which is also widely known as the Blossom algorithm. The time complexity of the original Blossom algorithm is $\mathcal{O}(|E||V|^2)$ where $|E|$ and $|V|$ are the number of edges and vertices, respectively. In the toric code set-up, which we have considered throughout the paper, a simple implementation gives $\mathcal{O}(n^4)$ (where $n = 2L^2$ is the total number of qubits) as $|V| \propto n$ (number of qubits) and $|E| \propto n^2$. Fortunately, the algorithm for MWPM has been improved and some suggest $\mathcal{O}(|V|^3)$ [43, 44] which gives $\mathcal{O}(n^3)$ for the toric code. We thus consider this as the worst-time complexity of the decoding problem using the MWPM decoder.

However, for decoding the toric code, an even more substantial speed up is possible by adopting the idea of locality – instead of constructing edges between *all* defects, one may construct edges only between nearby defects within some constant distance. Such an idea has been considered in Refs. [40, 45] and gave a visible speed-up for the decoding problem albeit this may potentially harm the threshold. PyMatching [34], which we have utilized for the MWPM decoder in this paper, could achieve $\mathcal{O}(L^{2.11})$ in benchmarks by combining this idea with an efficient C++ implementation of graph algorithms.

We present the threshold result for PyMatching in the upper panel of Fig. 6, where we find an error threshold of $p_{\text{err}} = 0.1542 \pm 0.0006$. This value is consistent with the previously established estimate of $3/2 \cdot p_{\text{err}}^{\text{indep}} \approx 0.1546$ (where $p_{\text{err}}^{\text{indep}} = 0.1031 \pm 0.0001$ is the threshold for the independent noise model estimated in Ref. [14]). This confirms that constructing edges only between nearby edges (as employed in PyMatching) barely shifts the threshold.

We have also explored using the MWPM decoder within the divide-and-conquer approach discussed in the main text (where the UF decoder is applied) in the lower panel of Fig. 6. Similar to our results for the UF decoder, we find a shift of the error threshold by some 10% to a value of

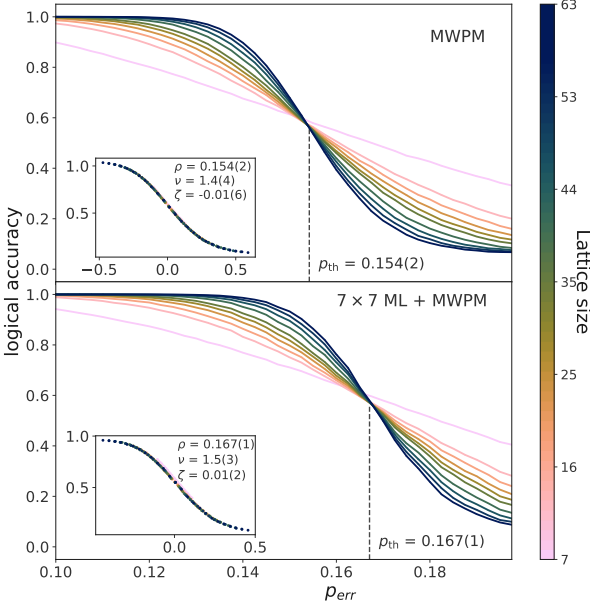


Figure 6. **Error threshold and scaling behavior** for the conventional minimum weight perfect matching (MWPM) algorithm (upper panel), and the machine learning assisted minimum weight perfect matching (ML+MWPM) algorithm (lower panel) for depolarized noise. The ML assisted algorithm shifts the error threshold by some 10%, from $p_{\text{err}} = 0.1542$ for the bare MWPM decoder to $p_{\text{err}} = 0.1671$ for the ML assisted MWPM algorithm (lower panel). The insets show a data collapse around these threshold values for different system sizes, consistently yielding a critical exponent of $\nu = 1.5(3)$.

$p_{\text{err}} = 0.1671 \pm 0.0005$. While these observations show that our divide-and-conquer approach can be employed with different ‘conventional’ decoders to achieve improved performance, we settled on the UF decoder for its algorithmic scalability bests all other conventional approaches.

Appendix D: Union-find (UF) decoder

Let us first briefly summarize the UF decoding algorithm [19]. For simplicity, we consider Z errors so that each syndrome (X_v) is assigned to a vertex (when considering X errors, the algorithm needs to be applied on the dual lattice). The first step of the UF decoder is to iteratively construct clusters such that each cluster contains an even number of syndromes. To do this, one first generates clusters where each one contains a single defect vertex. Then one pursues the following two steps iteratively until all clusters contain an even number of defects: (i) Extend all clusters a half-edge in all four directions (*Grow* step). (ii) When two clusters meet at an edge, one merges the two clusters (*Merge* step). When these iterations terminate, one can then use a peeling decoder [46] to infer the error corrections from the constructed clusters. To achieve an algorithmic scaling of $\mathcal{O}(na(n))$ (where $\alpha(n)$ is the inverse of Ackermann’s function [19]), one needs a disjoint-set data structure (which is also often called *union-find*) to maintain

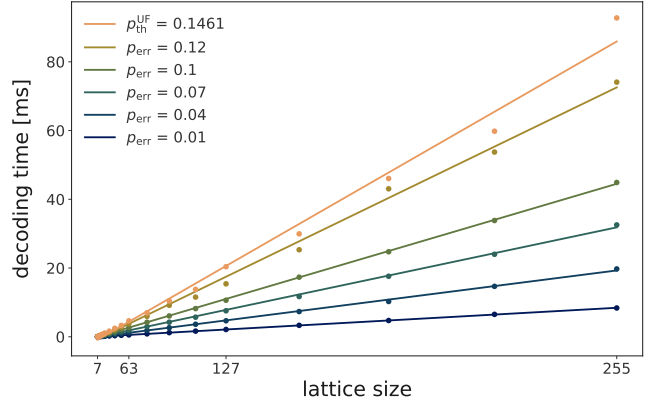


Figure 7. **Scaling of the UF decoder.** Average decoding time of our custom implementation of the UF decoder [33] as a function of linear lattice size. We find a *linear* scaling for a wide range of error rates (the lines are linear fits to the data as a guide to the eye). For the error rates near the threshold ($p_{\text{err}} = 0.12$ and p_{th} in this plot), we find deviations from the linear fit, which we believe to originate from rehashing operations, as our implementation relies on a *hash set* data structure to maintain border vertices of a cluster.

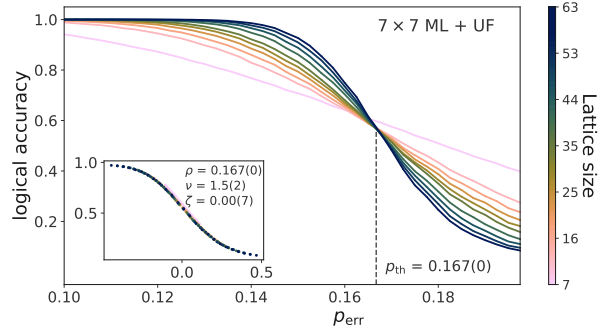


Figure 8. **Error threshold and scaling behavior** for the machine learning assisted union find (ML+UF) algorithm using a 7×7 subsystem mask. In comparison to the more time-efficient 5×5 subsystem mask of Fig. 2 in the main text, the larger subsystem mask applied here leads to a small shift of the error threshold to $p_{\text{err}} = 0.167(0)$. The insets show a data collapse around this threshold value for different system sizes, consistently yielding a critical exponent of $\nu = 1.5(2)$.

data of all clusters, as well as a clever updating scheme for boundary vertices for each cluster. For more details on these algorithmic details, we refer to the original paper [19].

For the UF decoder used in our divide-and-conquer algorithm, we have implemented a custom, open-source C++ code [33] of the union-find algorithm and the decoder. A thorough analysis of the decoding times of the bare UF decoder and its scaling with system size for different error rates are provided in Fig. 7. Similar to the results in Ref. [19], we find an almost perfect linear scaling of the UF decoder. Note that while the original implementation of the UF decoder has discussed only a specific error model (phase-flip with eraser errors) [19], we here present results for the depolarizing noise model used throughout this manuscript. Data for the error

title	date	QECC	noise model	p_{th}	d_{max}	algorithmic scaling
-------	------	------	-------------	-----------------	------------------	---------------------

conventional decoders (non-ML)

Analysis of quantum error-correcting codes: symplectic lattice codes and toric codes [14] (MWPM)	05/2004	TC	DP*	0.154*	63*	$\mathcal{O}(n^3)$ $\mathcal{O}(d^{2.11})$ (PyMatching [34])
Fast Decoders for Topological Quantum Codes [16] (RG-decoder)	02/2010	TC	DP	0.164	128	$\mathcal{O}(d^2 \log d)$ $\mathcal{O}(\log d)$
Almost-linear time decoding algorithm for topological codes [19] (UF-decoder)	09/2017	TC	DP*	0.146*	127*	$\mathcal{O}(n \cdot \alpha(n))$
General tensor network decoding of 2D Pauli codes [39] (TN-decoder)	01/2021	TC	DP	0.1881(3)	64	$\mathcal{O}(n \log n + n\chi^3)$

ML-assisted decoders

Decoding Small Surface Codes with Feedforward Neural Networks [21]	05/2017	SC	DP	~ 0.15	7	$\mathcal{O}(\text{MWPM})$
Neural Decoder for Topological Codes [22]	07/2017	TC	i.i.d bit flip	~ 0.110	6	$> \mathcal{O}(\text{MWPM})$
Deep Neural Network Probabilistic Decoder for Stabilizer Codes [23]	09/2017	TC	DP	0.164	11	$\gg \mathcal{O}(\text{MWPM})$
Neural network decoder for topological color codes with circuit level noise [24]	01/2019	CC	CLN	$\epsilon \sim 0.0023$	7	n.a.
Neural Belief-Propagation Decoders for Quantum Error-Correcting Codes [25]	05/2019	TC	i.i.d. X&Z	~ 0.07	10	n.a.
Quantum error correction for the toric code using deep reinforcement learning [26]	09/2019	TC	i.i.d. bit flip	~ 0.1	7	$\gg \mathcal{O}(n)$ (estimate)
Symmetries for a High Level Neural Decoder on the Toric Code [27]	10/2019	TC	DP	n.a.	7	$\mathcal{O}(\text{MWPM})$
Deep Q-learning decoder for depolarizing noise on the toric code [28]	05/2020	TC	DP	~ 0.165	7 (9)	$\gg \mathcal{O}(n)$ (estimate)
Reinforcement learning for optimal error correction of toric codes [29]	06/2020	TC	i.i.d bit flip	0.103	9	$> \mathcal{O}(\text{MWPM})$
Neural Network Decoders for Large-Distance 2D Toric Codes [30]	08/2020	TC	i.i.d. bit flip	~ 0.103	64	$> \mathcal{O}(\text{RG})$
Reinforcement learning decoders for fault-tolerant quantum computation [31]	12/2020	SC	i.i.d. bit flip & DP	n.a.	5	$\gg \mathcal{O}(n)$ (estimate)
Scalable Neural Decoder for Topological Surface Codes (this work)	01/2021	TC	DP	0.167	255	$\mathcal{O}(\text{UF})$

Table V. **Literature overview** summarizing key characteristics of a selection of ‘conventional’ decoders and ML-assisted decoders for different quantum error correcting codes (QECC) including the toric code (TC), the surface code (SC), and the color code (CC). For each decoder, we indicate the noise model (DP = depolarizing noise, i.i.d. = independent and identically distributed, CLN = circuit level noise), provide the error threshold p_{th} , the largest code distance tested d_{max} , and the algorithmic scaling in order of the total number of qubits n . The asterisk for the threshold values for the MWPM and UF decoders indicates that these numbers have been determined in this work.

threshold for this noise model for 5×5 subsystem mask are shown in Fig. 2 of the main manuscript. We additionally present finite-size scaling results with 7×7 subsystem mask in Fig. 8 where the threshold 0.167(0) is obtained.

Finally, we note that when the UF decoder is used in conjunction with the ML preprocessing step, we do *not* expect that the decoding time of the UF part will follow that of the bare UF decoder with a corresponding effective error rate (see, e.g., Fig. 3 of the main text). This is due to the fact that the errors, which remain after the ML decoding, exhibit a significant amount of *long-range* corrections, and thus need more *Grow* and *Merge* operations than independent i.i.d. noise cases. In fact, we have observed that, regardless of error rates,

the UF decoder part dominates the overall decoding time in our ML+UF scheme for larger system sizes.

Appendix E: Literature overview

To allow for a detailed comparison of our ML-assisted divide-and-conquer decoder presented in this manuscript with other decoding algorithms in the literature, in particular with regard to achievable error thresholds and algorithmic scaling, we provide a comprehensive overview of the existing literature in Table V above.